Experimental Studies of Hypersonic Shock Impingement on a Transpiration-Cooled Flat Plate

Imran Naved *, Tobias Hermann†, Chris Hambidge‡, and Matthew McGilvray§
University of Oxford, Oxford, England OX2 0ES, United Kingdom

Hypersonic vehicle design requires mitigation of the high heat fluxes present in regions of shock-wave boundary layer interactions. A candidate technology that may be applied locally to these regions is transpiration cooling. In this work, experiments were conducted in the Oxford High Density Tunnel at Mach 6.1 in both laminar and turbulent undisturbed boundary layer regimes where a 10° shock generator impinged a strong oblique shock wave onto a transpiration-cooled micro-porous injector. For the laminar boundary layer, due to the strength of the incident shock, a transitional shock-wave boundary-layer interaction region was formed with peak heating over 50 times greater than the nominal laminar level. Both nitrogen and helium were used as coolants. Relatively low levels of helium injection of 0.10 kg m^{-3}, for the transitional, and 0.14 kg m^{-3}, for the turbulent scenarios, respectively, were sufficient to reduce the heat transfer downstream of shock interaction to approximately 50% of the value without cooling. In fact, helium is highly effective with a similar cooling performance achieved as 8 times the equivalent mass flux of nitrogen. The experimental data are correlated and both the turbulent and transitional shock impingement scenarios display a similar trend of reduced surface heat transfer with higher blowing parameters. Empirical fits are proposed which may be used for initial systems design.

Nomenclature

B_h	Blowing parameter
c_p	Specific heat capacity, J kg^{-1} K^{-1}
F	Blowing ratio, $(\rho_f u_f)/(\rho_e u_e)$
K_D	Darcy coefficient, m^2
K_F	Forchheimer coefficient, m
M	Mach number
M	Molecular weight, g mol^{-1}

*D.Phil. Student, Oxford Thermofluids Institute, University of Oxford, AIAA member
†Departmental Lecturer, Oxford Thermofluids Institute, University of Oxford, AIAA member
‡Research Assistant, Oxford Thermofluids Institute, University of Oxford, AIAA member
§Associate Professor, Oxford Thermofluids Institute, University of Oxford, AIAA member

$\dot{m}_f$	Mass flux, $\mathrm{kg\,s^{-1}\,m^{-2}}$
$\dot{q}$	Heat flux, $\mathrm{W\,m^{-2}}$
Re	Reynolds number
St	Stanton number
T	Temperature, K
TPS	Thermal protection system
u	Velocity, $\mathrm{m\,s^{-1}}$
x	Distance from the leading edge, m
y	Lateral distance from the model centreline, m
μ	Viscosity, $\mathrm{Pa \cdot s}$
ϕ	Porosity
ρ	Density, $\mathrm{kg\,m^{-3}}$

Subscript

0	Uncooled reference
2	Post oblique shock, see Fig, 1
3	Post re-compression shock, see Fig, 1
e	Gas at boundary layer edge
f	Coolant fluid
L	Shock impingement location
r	Recovery
w	wall
∞	Freestream value upstream of shock interaction

I. Introduction

Shock-wave-boundary-layer interactions (SWBLIs) often take place on deployed control surfaces, at the juncture between vertical fins and the fuselage, and the inlets of hypersonic vehicles [1]. The impinging SWBLIs can lead to harsh adverse pressure gradients which may result in boundary layer separation with correspondingly high surface pressures and heat loads. Depending on the state of the incoming boundary layer as well as the shock strength, SWBLIs may be broadly divided into three types based in the state of the boundary layer downstream of shock impingement: laminar, transitional, and turbulent. The second of these types generally occurs where the incoming boundary layer is laminar but the free-stream Reynolds number is in the upper end of the laminar regime and the strength of the

incident shock causes the boundary layer to separate and rapidly transition to turbulence[2]. Hypersonic transitional SWBLIs can result in significantly greater peak surface heat transfer than laminar or turbulent interactions [3–6] and are a phenomenon of great interest, especially for the outer surfaces of hypersonic cruise vehicles where in many cases the boundary layer is laminar up to the shock interaction. This is a particular concern for hypersonic cruise vehicles wherein the actuation of control surfaces may lead to an SWBLI interaction, triggering transition or even boundary layer separation and leading to very high off-design thermal and pressure loads. Turbulent interactions on the other hand are common in the walls of scramjet combustors [1] which whilst promoting mixing, can result in very high localised heat loads and dynamic pressure which need to be mitigated.

Designing a thermal protection system (TPS) that is able to withstand these high heat fluxes is challenging. One candidate is transpiration cooling which is an active thermal protection system that can be applied to hypersonic vehicles. This involves passing a cool fluid through a porous material into the external boundary layer. Cooling is achieved through a combination of the coolant creating a thin film which thickens the boundary layer and insulates the wall from the hot external gas, internal convection between the coolant and porous medium, and, in certain cases if an inert gas is used, the coolant film can protect the wall from surface oxidation and catalytic recombination. The advantage of transpiration cooling is the flexibility of using this technique for a wide range of free-stream conditions. In addition, the introduction of the low-velocity coolant gas reduces the velocity gradient in the boundary layer, and therefore the skin friction, which for internal walls of combustion chambers, is a major contribution to engine drag [1].

However, this is balanced out by the additional complexity budget introduced to implement this system. In particular, transpiration cooling is a good candidate for cooling local hot spots caused by SWBLIs as this TPS system may be applied locally to regions where these interactions are likely to occur. However, a critical aspect of these flows is whether the coolant layer can withstand the disturbances caused by the shock wave and remain intact throughout the interaction region. If the coolant layer remains intact, then it is likely that a marked reduction in peak heating is possible [7].

There are limited previous experimental studies exploring the effectiveness of transpiration cooling for SWBLIs, especially at hypersonic conditions. The most extensive experiments were carried out by Holden and Sweet [7] in the 1990s where the surface heat transfer and pressure on a flat plate with a transpiration-cooled wall in turbulent hypersonic flow was characterised by a range of varying blowing rates and incident shock strengths. Nitrogen and helium were used as coolants and a range of shock generator angles between 5-10° were employed to generate the incident shock. It was found that the interaction region between the incident shock and the low-momentum transpiration-cooled boundary layer did not result in a significant increase in the size of attached or separated interaction regions, and did not result in significant flow-field distortions above the interaction region. Thus, the heating downstream of the shock-impingement point could easily be reduced to values without shock impingement by a relatively small increase in transpiration cooling in this region. For supersonic flows, Strauss et al. [8] found that impinging a shock with a 9.3° ramp angle shock

generator at Mach 2.5 led to only moderate reductions ($\approx 5\%$) in cooling efficiency (i.e. $\frac{T_r - T_w}{T_r - T_f}$) compared to the case without impingement. This is a promising result though the authors note that hotspots due to shock-boundary layer interaction on the porous wall can be an issue, with locally high thermal loads and, therefore, an increase in the risk of structural failure in the porous material, especially so if the wall segment is thin.

The work reported in this paper presents experimental results concerning shock impingement onto a transpiration-cooled porous wall at Mach 6.1 laminar and turbulent conditions. In this study, a 10° shock generator was installed to generate a strong oblique shock to impinge onto a flat plate model. The effectiveness of transpiration cooling for a transitional SWBLI case has never been reported before even though some of the highest heat fluxes occur in this case. The surface heat transfer of the transpiring porous injector is characterised using high-speed infrared thermography which spatially resolves the 2D flow structures at the wall and crucially, the non-intrusive nature of this technique enables measurements directly on the porous injector without impeding or otherwise disturbing the coolant outflow. Infrared thermography has been previously tested and validated for transpiration-cooled surfaces in hypersonic flows by Naved et al. [9] and this technique is the basis for the heat transfer measurements presented in this paper.

II. Experimental Methodology

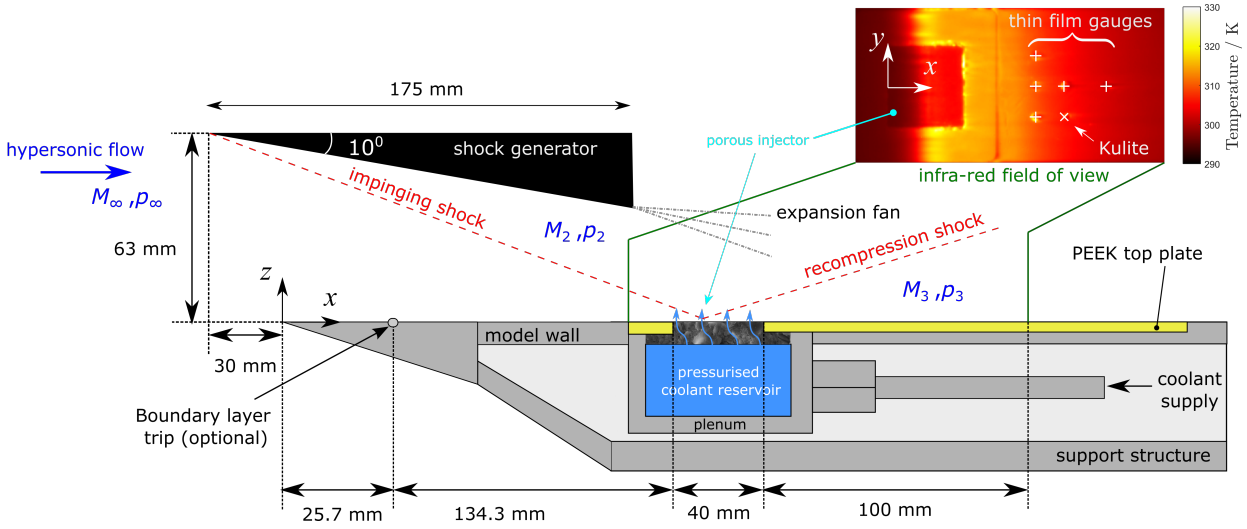

Fig. 1 Cross-sectional schematic of the flat plate model with the position of the shock generator and the field of view for infrared thermography. Not to scale. The flat plate is mounted vertically in the test section as indicated by Fig 2.

A. Experimental Model

The experiments were conducted on a flat plate model at 0° angle of attack as described in Naved et al. [10]. Figure 1 shows a cross-section of the experimental model. A porous injector of 39.5 x 39.5 mm was placed 160 mm downstream of the sharp (radius < 0.1 mm) leading edge. A plenum is located underneath the injector and pipework is placed to feed

the injection gas to the injector. The temperature and pressure in the plenum were measured by a fast response K-type thermocouple (⌀0.0762 mm) and a Kulite pressure transducer (HEL-375-35BARA). Downstream of the porous injector, the model features a 340 mm long PEEK surface for downstream infrared measurements. For a secondary verification of the surface heat transfer, 13 quartz-based platinum individual thin film gauges were mounted both upstream and downstream of the porous injector. Finally, 3D printed trips were added to a pocket 25.7 mm downstream of the leading edge to aid transition for the turbulent test cases. A diamond transition trip was used with a span-wise length of 90 mm and a height of 0.1 mm. A flush insert was used for the cases where a laminar undisturbed boundary layer was desired.

In addition, the surface static pressure was measured using two surface-mounted Kulite pressure transducers (XCS-093-5A). The freestream total temperature was measured prior to these experiments using differentially heated aspirated thermocouples. The measured data was acquired using a National Instruments PXIe-8135 controller with one PXIe-6368 card. A sample rate of 125 kHz was used to record all signals of the measurement which includes model and wind tunnel instrumentation. A separate in-house heat transfer amplifier unit, HTA5, is also used for thin film gauge data acquisition. This forms a stand-alone unit, run at a matching sample rate to the main DAQ system.

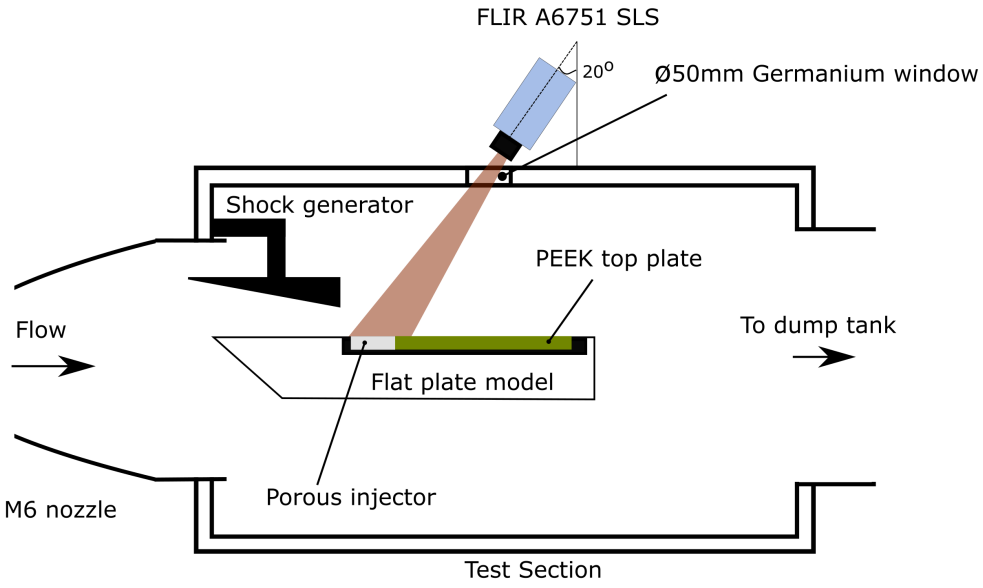

Fig. 2 Top view of the experimental model in the test section.

Primarily, surface heat transfer measurements were acquired using infrared thermography and a schematic of the optical setup is shown in Fig. 2. The experimental test piece was orientated in a vertical configuration such that the field of view (FoV) of the IR camera is nearly normal to the model surface. The FLIR A6751 SLS long-wave infrared (LWIR) camera with a wavelength band of 7.5-11μm was used for these experiments. The experimental model was viewed through a 50 mm coated Germanium window and the camera was operated at a windowed spatial resolution of 256 x 320 at a frame rate of 400 Hz. This results in approximately 15 frames over the steady tunnel test time.

Table 1 Properties of porous METAPOR CE170 and PEEK. The thermal properties (ρ,c_p,k) were measured by Netzsch Instruments and the emissivity, ε, was measured using an in-house benchtop setup [9]

Parameter	METAPOR CE170	PEEK
Thickness, L / mm	7	10
Porosity, ϕ	0.20	-
Density, ρ_s / kg m^{-3}	1710	1310
Thermal Conductivity, k_s / W m$^{-}K^{-1}$	1.662	0.25
Specific Heat Capacity, $c_{p,s}$ / J kg^{-1} K^{-1}	1177	1201
Thermal Effusivity, ($\sqrt{\rho c_p k}$) / Jm^{-2}K^{-1}s$^{-0.5}$	1565	627
Darcy Coefficient, K_D / m^2	$2.52 \cdot 10^{-13}$	-
Forchheimer Coefficient, K_F / m	$1.08 \cdot 10^{-8}$	-
Emissivity, ε	0.95	0.93

The porous injector used for these experiments was the METAPOR CE170 which is a commercially available micro-porous material made of aluminium hydroxide bonded to a resin system (pore diameter 20 μm). The properties of both METAPOR CE170 and PEEK are available in Table 1. Due to a lack of available manufacturer data for the thickness of the porous injector used for these experiments and to determine the localised permeability for the relatively small samples used in the experiment (39.5 x 39.5 x 7 mm), the outflow and permeability of the porous injector were measured according to the procedure detailed by Ifti et al. [11]. This was completed pre and post-experiment and both measurements were within the uncertainty bounds of the permeability measurement - i.e. there was no significant difference between the two measurements.

The 10° shock generator deflects the flow by 17° and is positioned above the main plate such that the inviscid shock impingement position is approximately 165 mm from the leading edge. The wedge was manufactured from a single block of aluminium, with a length of 175 mm and width of 200 mm and was mounted onto the test section wall. The width of the shock generator was maximized in order to minimize 3D effects on the 100 mm wide flat plate. The resulting inviscid shock strength at M_∞ = 6.1 is p_2/p_∞ = 3.73.

B. Heat transfer measurements

The surface heat flux was primarily measured by employing infrared thermography with additional individual thin film gauges to support and validate the infrared measurements. A series of calibration steps, further detailed in Ref. [9], were followed to obtain quantitative transient temperature maps of the flat plate surface including the transpiration-cooled injector from the raw infrared signal.

1) Multipoint calibration: Firstly, a multipoint calibration was carried out in-situ using a black body calibrator (CI-Systems SR-33-7 infrared calibrator) to relate the camera raw signal to the true black body temperature inside the wind tunnel test section. This step calibrates the camera and optical system by correcting any detector

or optical system spatial non-uniformity or offsets.

2) Emissivity measurement: Secondly, to relate the black body temperature to the true material temperature, a material emissivity measurement was performed pre-experiment by using a bench-top setup. The measured emissivity values for both the porous injector and the PEEK surface upstream and downstream of the injector are recorded in Ref. [9].
3) Image Processing: Finally, the images were spatially transformed to a rectangle that represents the physical geometry and passed through an image stabilisation algorithm prior to final post-processing.

After the corrected temperature profile, ΔT, was obtained the heat flux, $\dot{q}_w$, was determined by applying the impulse response method of Oldfield [12] employing the local material thermal properties of METAPOR CE170 (porous injector) and PEEK (the remainder of the flat plate), respectively. A fully coupled transpiration-cooled impulse response method such as in Hermann et al. [13] was not required as the convective heat transfer process between the coolant fluid and porous solid was accounted for by the calibration procedure. Further justification for this assumption and details of the calibration process are presented in Ref. [9].

C. Flow conditions and parameters

Table 2 Free-stream and post-recompression shock flow conditions. The post-recompression shock values are calculated from isentropic relations.

Parameter	Laminar		Turbulent	
	Freestream (∞)	Post-recompression shock (3)	Freestream (∞)	Post-recompression shock (3)
Pressure, p / Pa	786	8413	1985	21246
Temperature, T / K	49.6	107.8	44.0	95.6
Velocity, u / m s^{-1}	861	791	811	745
Density, ρ / kg m^{-3}	0.0552	0.272	0.157	0.774
Mach Number, M	6.1	3.80	6.1	3.80
Unit Reynolds Number Re_u / m^{-1}	$13.4{\cdot}10^6$	$28.2{\cdot}10^6$	$40.5{\cdot}10^6$	$84.8{\cdot}10^6$
Estimated boundary layer height, δ_{99}/ mm at x = 160 mm	2.36	-	4.44	-

The experiments were conducted in the Oxford High Density Tunnel (HDT) at the Oxford Thermofluids Institute operated in Ludweig tube mode. A detailed description of the facility may be found in Refs. [14, 15]. The Mach 6 nozzle was selected and two different freestream conditions were chosen to achieve both laminar and turbulent boundary layer states at the porous injector. The free-stream properties are calculated from measured stagnation pressures, pitot pressures, and temperatures using isentropic relations. The viscosity was determined using Keyes model [16] and Table 2 presents an overview of the flow conditions.

For direct comparison with previous investigations of transpiration-cooled walls without shock impingement, the experimental heat fluxes are expressed as a Stanton number which is based on the free-stream conditions upstream of the shock impingement

$$St = \frac{\dot{q}_w}{\rho_\infty u_\infty c_p (T_0 - T_w)} \tag{1}$$

where $\dot{q}_w$ is the heat flux at the wall, ρ_∞ is the free-stream density, u_∞ is the free-stream velocity, c_p is the specific heat capacity at constant pressure, T_0 is the total temperature and T_w is the wall temperature. Due to a lack of information regarding the local recovery factor in the shock interaction region as well as to maintain consistency with the aforementioned experiments conducted by Holden and Sweet [7], the more conventionally used recovery temperature is replaced by the total temperature in the equation above.

The blowing ratio, which is defined as the ratio of the coolant mass flux to the free stream mass flux at the boundary layer edge, is determined from the measured plenum and free-stream pressures and temperatures according to the Darcy-Forchheimer equation

$$\frac{p_f^2 - p_e^2}{2LR_f T_f} = \frac{\mu_f \dot{m}_f}{K_D} + \frac{\dot{m}_f^2}{K_F} \tag{2}$$

where the values of the permeability coefficients, K_D and K_F are given in Table 1 for the METAPOR CE170 injector used in this study. The free stream mass flux at the boundary layer edge may be defined either upstream of injection, $\rho_\infty u_\infty$, or downstream of the re-compression shock, $\rho_3 u_3$. Thus two blowing ratios may be defined

$$F = \frac{\dot{m}_f}{\rho_\infty u_\infty} = \frac{\rho_f u_f}{\rho_\infty u_\infty} \tag{3}$$

and

$$F_3 = \frac{\dot{m}_f}{\rho_3 u_3} = \frac{\rho_f u_f}{\rho_3 u_3} \tag{4}$$

where the subscript 'f', '∞', and '3' denote the coolant, the boundary layer edge value upstream of the shock interaction region, and the boundary layer edge value downstream of the re-compression shock. The boundary layer edge values downstream of the re-compression shock ('3' in Fig. 1) are found by applying oblique shock relations across the impinging and re-compression shocks.

As the surface pressure rises rapidly over the porous injector, there is a risk that the constant mass flux assumption does not hold over the injector as, from the Darcy-Forchheimer equation, the injected mass flux depends both on the plenum pressure and surface pressure. To assess whether this occurs, the lowest plenum pressure tested for the turbulent condition (where the surface pressure is the highest) is 2.7 bar. The corresponding surface pressure downstream of the

re-compression shock (from Table 2) is 0.212 bar - just under 8% of the plenum pressure - whilst upstream of the shock, it is 0.0198 bar. Applying the two surface pressures to the Darcy-Forchheimer equation, the difference in coolant mass flux between the two scenarios is less than 0.45 %. Higher plenum pressures and lower surface pressures would lead to an even smaller difference. This value is within the error of mass flux measurement and, therefore, it may be assumed that the injected mass flux is constant within reasonable accuracy over the porous injector for all the test cases presented in this work.

Table 3 Overview of blowing cases at both laminar and turbulent conditions. F is the blowing ratio based on the boundary layer edge conditions upstream of shock impingement, '∞', and F_3 is the blowing ratio based on the boundary layer edge conditions downstream of shock impingement, '3'. T_f and p_f are the measured coolant temperature pressure.

Coolant	Boundary layer state	$\dot{m}_f$ / kg m^{-3}	F / %	F_3 / %	T_{res} / K	P_{res} / kPa
N_2	Laminar	0.11	0.24	0.052	293	108
N_2	Laminar	0.26	0.55	0.13	292	177
N_2	Laminar	0.81	1.71	0.38	293	389
He	Laminar	0.014	0.030	0.0070	291	100
He	Laminar	0.022	0.046	0.010	291	124
He	Laminar	0.042	0.088	0.019	292	173
He	Laminar	0.10	0.21	0.047	292	279
N_2	Turbulent	0.48	0.38	0.084	292	268
N_2	Turbulent	0.74	0.58	0.13	294	365
He	Turbulent	0.056	0.044	0.0097	291	202
He	Turbulent	0.14	0.11	0.024	291	335

Table 3 presents an overview of all the cases considered in this study. The quoted values of the blowing ratio in the subsequent results section are all based on F, the blowing ratio based on the boundary layer edge values upstream of impingement. The corresponding blowing ratios downstream of the re-compression shock may be read off the table. Some of the values of F, especially for the laminar cases, are very high compared to previous experiments in a similar setup [10]. This is due to the higher free-stream mass flux post-recompression shock which then requires higher coolant mass fluxes to result in a significant heat transfer reduction.

III. Results and discussion

For the targeted laminar and turbulent conditions on the flat plate, it is necessary to first ascertain that the correct boundary layer state is achieved before shock impingement. Figure 3 presents the span-wise averaged surface Stanton number (between y = -15 to 15 mm) for both the laminar and turbulent shock impingement cases as well as the equivalent without shock impingement. Without impingement, the boundary layer remains laminar and turbulent, respectively, within the porous domain. For the laminar boundary layer, transition occurs from x = 200 mm onwards. Overall, there is

a great agreement to within 5% with the flat plate correlations of Eckert [17].

Once the shock generator was installed, the generated impinging shock interacts with the flat plate on the porous injector. The SWBLI increases the boundary layer thickness and there is likely to be at least some flow separation due to the shock intensity and boundary layer state. The expansion waves from the rear of the shock generator increase the Mach number and interact with the reflected shock. These expansion waves impinge onto the boundary layer far downstream of the SWBLI region and do not influence the interaction region. The inviscid shock impingement location and the position where expansion waves emanating from the end of the shock generator interact with the model surface are marked in Fig. 3. The position of the expansion fan correlates well with the position at which the surface heat transfer begins to reduce agreeing with previous experiments for a turbulent boundary layer by Schluein [18].

For the incoming laminar boundary layer, a clear location of peak heating is located at $x \approx 178$ mm. After that point, the heat flux reduces gradually plateauing from 190-210 mm to $St = 0.01$. This curve is characteristic of a transitional shock interaction where due to the relatively high Reynolds number at the shock impingement location ($Re_L > 2.4 \cdot 10^6$) and the large shock generator angle (10°), shock-induced transition occurs leading to significantly higher heating rates than even purely turbulent flows [6]. As noted by Currao et al. [3] for a similar configuration (Mach 5.8, shock generator angle of 10° and $Re_u = 7 \cdot 10^6$ m^{-1}), shock-induced transition caused separation to occur well ahead of the shock impingement location with the reattachment region very close to the inviscid shock impingement location. The fact that peak heating rates are well above the fully turbulent level suggests that a similar flow topology was attained in these experiments with the transition to turbulence occurring prior to the inviscid shock impingement point.

Following previous flowfield studies by Schluein [18], for a fully turbulent incoming boundary layer, the interaction of the oblique shock with the boundary layer is likely to cause a separation zone upstream of the shock impingement point. For large wedge angles (i.e. greater than 10°), it is noted that whilst the skin friction decreases in the vicinity of the separation point, the heat flux increases. The increase in heat flux is present in these experimental heat transfer measurements (Fig. 3) and is indicative of the complex non-equilibrium behaviour in such turbulent interacting flows where the Reynolds analogy between momentum and heat transfer is not valid. Such an increase in the heat flux rate for separated flow regions has also been observed in other studies of two-dimensional interactions [5]. The amplification of turbulence in the boundary layer and in the external flow due to the shock wave interaction, as well as the higher surface pressure and density due to the stronger separation shock (compared to similar interactions in purely laminar flows) are possible explanations for the observed increase in the surface heat transfer in the interaction region. From Fig. 3, a peak of $St \approx 0.0055$ is reached towards the end of the porous injector for the turbulent SWBLI. This is closely in line with previous investigations with shock impingement at Mach 5 turbulent flow by Schülein [18].

The peak heating rates for laminar, turbulent, and transitional shock impingement regions have been correlated by Hung and Barnett [4]. It was found that when $Re_L > 5 \cdot 10^5$ the boundary layer flow is sufficiently disturbed that SWBLI disturbance promotes transition. The expressions for transitional and turbulent flows are

$$\left[\frac{St}{St_0}\right]_{\max} = 0.468 \cdot (Re_L \cdot 10^{-6}) \cdot \left(\frac{p_3}{p_\infty}\right)^{1.13} \qquad \text{Transitional} \tag{5}$$

$$\left[\frac{St}{St_0}\right]_{\max} = 0.13 \cdot \left(\frac{p_3}{p_\infty}\right)^{0.8} \qquad \text{Turbulent} \tag{6}$$

where, for these experiments, $\left[\frac{St}{St_0}\right]_{\max}$ = 34.9 for the transitional and 6.7 for the fully turbulent scenarios. As shown by Fig. 3, both values under-predict the experimentally measured peak heating. This has also been observed by Heffner et al. [19] and Holden and Sweet [7] but, nonetheless, the correlations are useful to benchmark the experimental data.

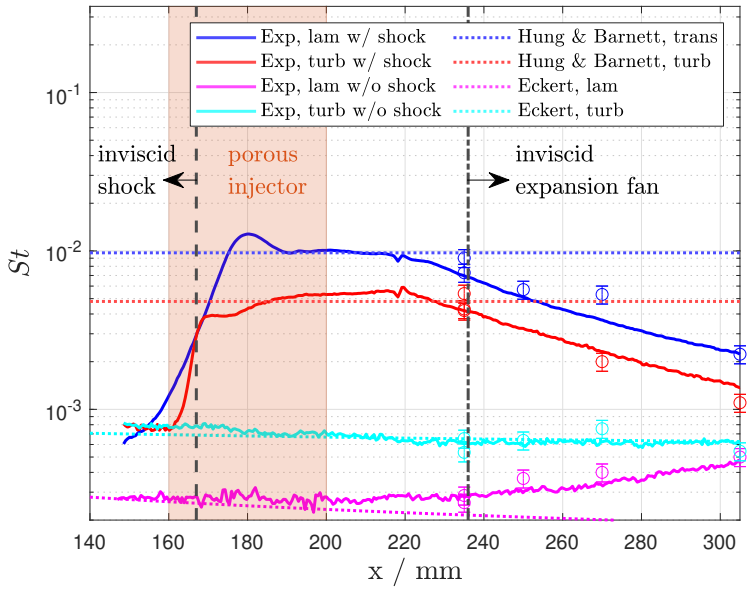

Fig. 3 Span-wise averaged surface Stanton number (averaged between y = -15 to 15 mm) of the uncooled shock impingement and unshocked cases at both laminar (Re_u = 13.4·10^6 m^{-1}) and turbulent (Re_u = 40.5·10^6 m^{-1}) conditions. The circular points represent thin film gauges. The discontinuity at x ≈216 mm is due to the joint between the model and the plate that holds the injector.

The following experimental results with the inclusion of transpiration cooling are discussed in terms of the boundary layer state downstream of shock impingement, i.e. transitional or turbulent. The experimental results are split into three sections. The first section details the case where the strong shock impinges onto a laminar boundary layer with nitrogen and helium injection, the second concerns the respective turbulent cases, and in the final section correlations are developed to predict the effectiveness of transpiration cooling for turbulent and transitional shock interaction regions for system design purposes. The results are normalised either in relation to St_0, the Stanton number without shock impingement when F = 0% or $St_{0,s}$, the Stanton number with shock impingement when F = 0%.

A. Transitional

Contour plots of the Stanton number ratio between the shocked and unshocked experimental data (St/St_0) are plotted in Fig 4. For the uncooled case, a rapid rise in heat transfer occurs across the injector peaking at over 50 times higher than the nominal laminar boundary layer without injection. Clear span-wise periodical variations are present on the porous injector surface. These have also been observed by Currao et al [3] for similar transitional SWBLIs who attributed them to Görtler instability and the associated contra-rotating stream-wise vortices. Whilst these vortices likely do not cause transition themselves, they lead to other forms of instability that eventually result in transition [20]. With coolant injection, there are prominent 'cold' patches for the helium case downstream of impingement at approximately x = 195 mm. This may be attributed to non-uniformities in the coolant outflow for this porous injector [10]. These patches are not present for the nitrogen case likely due to the higher outflow velocity of helium for a given injected mass flux (due to its lower density) exacerbating local flow structures.

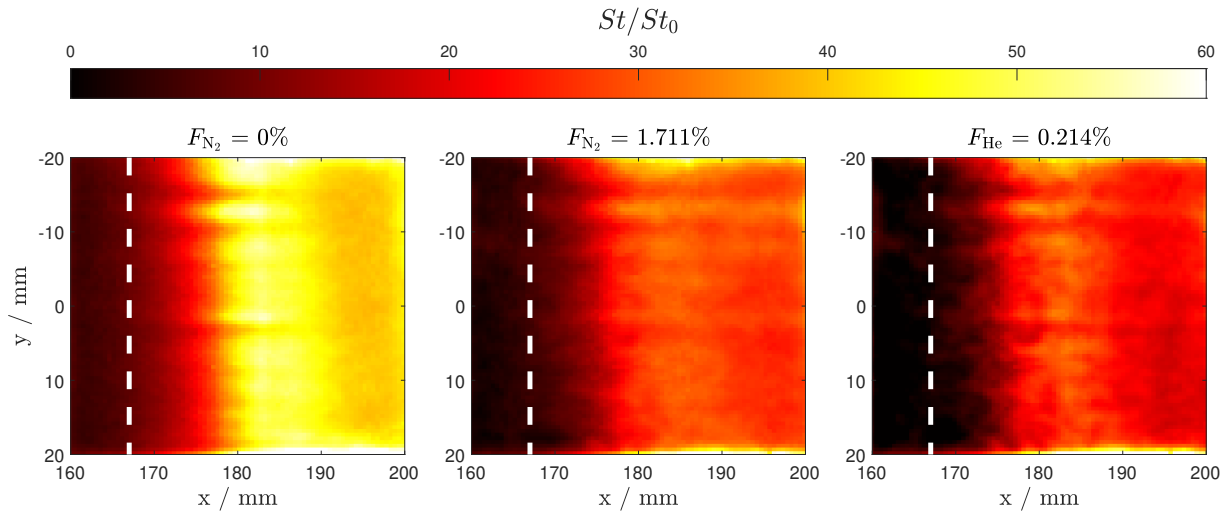

Fig. 4 Contour plots of three transitional cases normalised against the nominal laminar case without shock impingement (St/St_0). The white dashed line indicates the inviscid shock impingement location.

Figure 5 shows spanwise averaged (between y = -15 to 15 mm) heat transfer reduction curves based on either the uncooled case without shock impingement, St_0, or the uncooled case with shock impingement, $St_{0,s}$. The contours show a slightly asymmetric Stanton number distribution relative to the freestream, especially for the uncooled case. This is likely due to a slight misalignment of the shock generator relative to the flat plate whilst with the inclusion of cooling, the blockage effect of the coolant on the SWBLI smoothes out the asymmetry. From Fig 5a, it is clear that both nitrogen and helium injection have little effect on the overall stream-wise heat transfer profile but rather lower the surface heat flux over the entire injector. For the highest nitrogen injection, the value of St_s/St_0 is reduced to below 30 which corresponds to over 60% less heat transfer compared to the unshocked case. Considering Fig. 5b, it is interesting to note the very steep reduction in heat transfer upstream of impingement. This is likely due to a combination

of the lower surface pressures (leading to a higher local blowing ratio) upstream of the interaction region (denoted approximately by the inviscid shock line) and the laminar nature of the flow before the strong separation caused by the shock. Downstream of the interaction region ($x > 180\,\text{mm}$), the heat transfer reduction is very flat, characteristic of previous measurements of transpiration cooling in turbulent flows without SWBLI [10]. For helium injection, a blowing ratio of 0.214% essentially achieves a similar $St_s/St_{0,s}$ downstream of the shock interaction ($x > 180\,\text{mm}$) as nitrogen with 1.711%; i.e. only 12.5% the mass flux of helium is required to achieve the same cooling efficiency as nitrogen, highlighting the increased effectiveness of helium for these cases. A combination of the higher specific heat capacity of helium which provides the capacity to absorb roughly 5 times greater quantities of heat than nitrogen for the same mass flow rate, and the lower molecular weight likely contribute to the increased effectiveness. As helium's molecular weight is lower than that of nitrogen, a higher plenum pressure is required to achieve the same mass flux through the injector. This leads to two differences at the exit: helium exits at a higher velocity due to its lower density at a given edge pressure, p_e, and helium contain more gas particles than nitrogen since a higher plenum pressure results in a higher mole number; i.e., a higher mole number leads to a larger volume of helium at the exit. In combination, these two effects result in seven times the higher volumetric flow rate of helium when its mass flow rate is matched with nitrogen. This likely thickens the boundary layer at the shock impingement location and results in a reduced wall temperature gradient.

For $F_{N_2} = 1.711\%$, a negative Stanton number is recorded at $x = 163\,\text{mm}$. For very high blowing ratios, where the boundary layer close to the wall is almost entirely comprised of coolant, a negative Stanton number may arise when the coolant gas layer is rapidly accelerated due to the shear stress of the external flow. This would lead to the coolant gas itself establishing a velocity profile akin to the external boundary layer which leads to a dissipation of thermal energy. Since the injected coolant gas starts at near-zero stream-wise velocity close to the wall and the coolant temperature is very near to the wall temperature (Table 3), the total temperature of the coolant layer is similar to the wall temperature. This means that the effective driving temperature of the wall heat transfer (generally represented by the recovery temperature) has to be lower than the wall temperature and therefore a negative heat flux (and therefore Stanton number) may occur. A similar phenomenon has been observed by Ifti et al. [21] for a transpiration cooling in a laminar hypersonic boundary layer and by Keller et al. [22] and Hombsch and Olivier [23] for slot injection in supersonic and hypersonic flows.

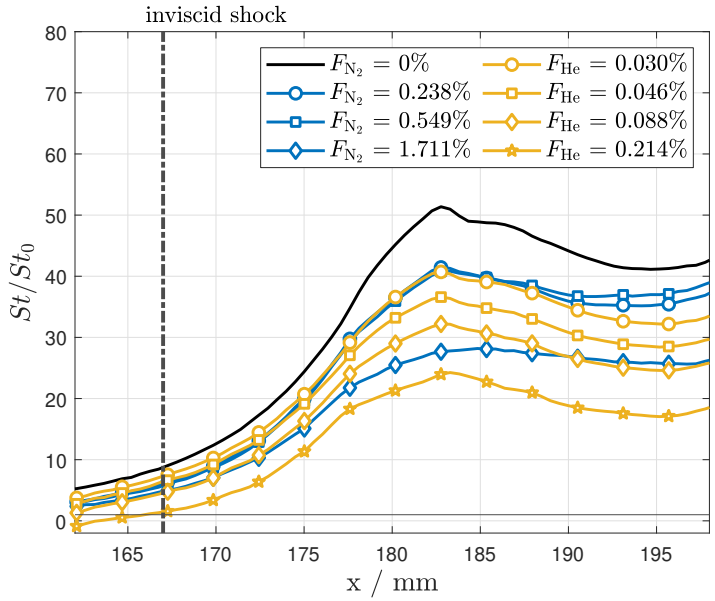

(a) In terms of the heat transfer reduction relative to the uncooled case without shock impingement, St/St_0.

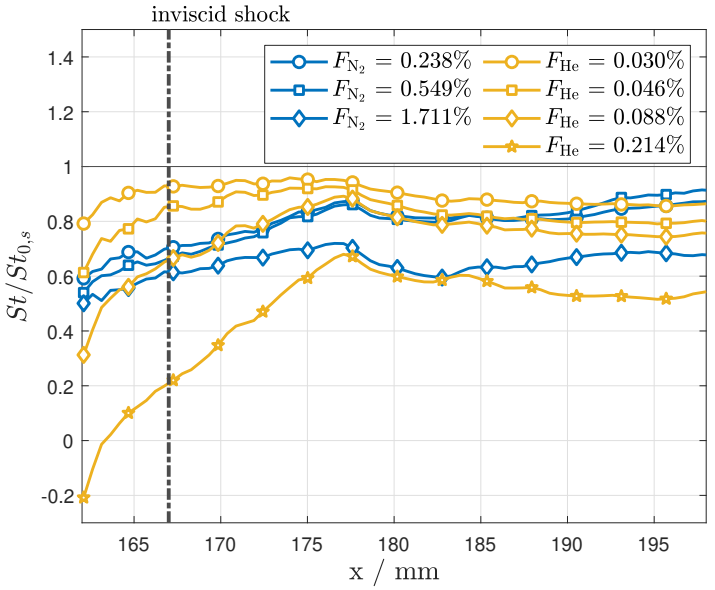

(b) In terms of the heat transfer reduction relative to the uncooled case with shock impingement, $St/St_{0,s}$.

Fig. 5 Span-wise averaged Stanton number ratio between y = -15 to 15 mm for the transitional condition. The data is constrained to the range of x = 162-198 mm to disregard non-physical rises at the intersection between the injector and the cover plate.

B. Turbulent

The turbulent cases manifest a markedly different profile from the transitional cases. Fig 6 shows three contour plots for the turbulent flow condition normalised against the nominal turbulent case without shock impingement. There is a

sudden jump at ≈ 165 mm for the uncooled case and then a shallower gradient until the end of the porous injector at x = 200 mm. With coolant injection, a consistent 'smoothing' of the heat transfer profile in the stream-wise direction over the injector is observed with higher heat transfer upstream of the shock impingement location for the nitrogen and low helium cases. However, with sufficient injected mass flux, such as for helium injection at F = 0.110%, the heat transfer upstream also reduces to below the uncooled case. Once again, similar to the transitional cases, significant spatial non-uniformities are present in the helium case.

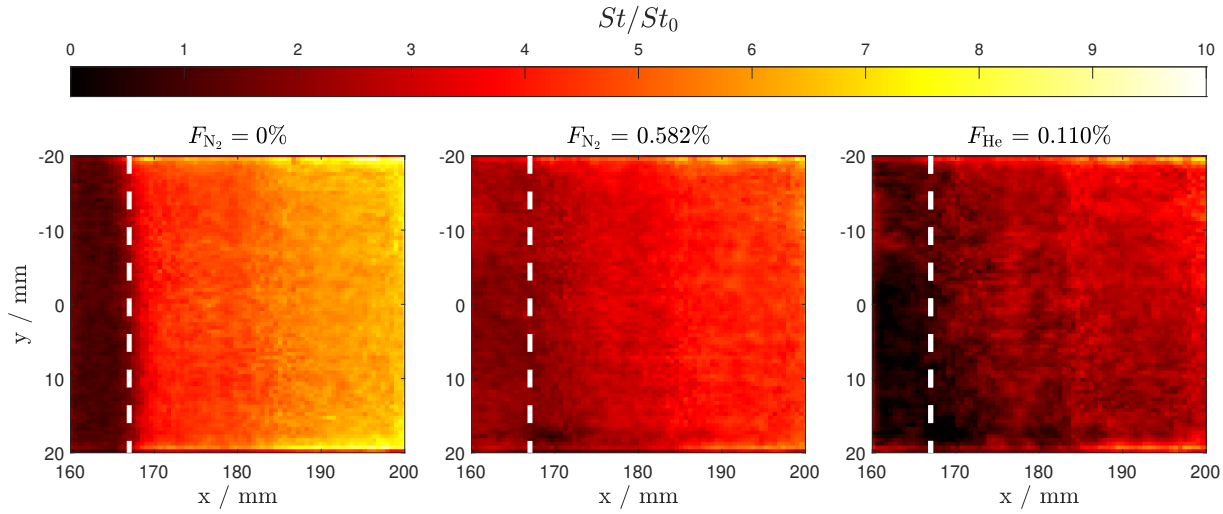

Fig. 6 Contour plots of three turbulent cases normalised against the nominal turbulent case without shock impingement (St/St_0). The white dashed line indicates the inviscid shock impingement location.

From Fig. 7b, it is observed that on and upstream of the shock impingement location, the heat transfer enhancement is over double the nominal uncooled case. This effect has not been reported previously in literature though it may be due to the introduction of the subsonic coolant layer moving the separation bubble caused by the impinging shock further upstream compared to the uncooled case. Heat transfer rates are particularly strong in the vicinity of the point at which the separated flow re-attaches and an earlier reattachment point would shift the rapid change in heat transfer further upstream [24]. Further computational and experimental studies would be valuable to provide insight. Downstream of impingement, a very similar profile is present as the transitional cases discussed previously. This confirms that a fully turbulent region remains downstream of the interaction and the flat profile is similar to cases where transpiration is applied to turbulent flow without impingement. Once again helium is significantly more effective than nitrogen. A blowing ratio, F, of 0.582% of nitrogen is sufficient to reduce peak heat transfer to just under 70% of the uncooled case whilst only 0.110% of helium is sufficient to reduce it to under 50%. Helium is approximately 8 times more efficient for the same blowing ratio of nitrogen which is a similar ratio to the transitional cases described previously.

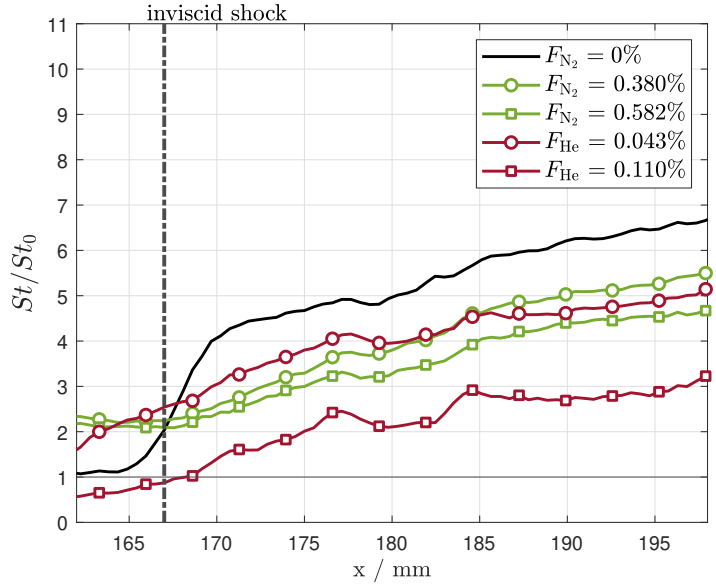

(a) In terms of the heat transfer reduction relative to the uncooled case without shock impingement, St/St_0.

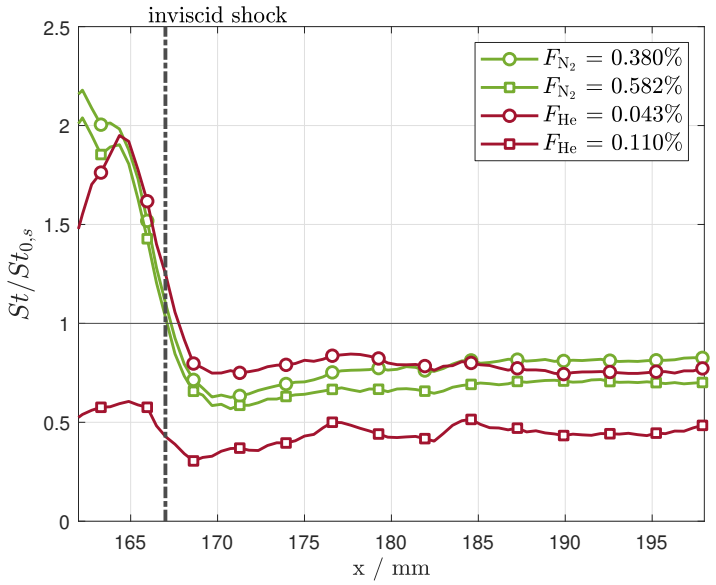

(b) In terms of the heat transfer reduction relative to the uncooled case with shock impingement, $St/St_{0,s}$.

Fig. 7 Span-wise averaged Stanton number ratio (averaged between y = -15 to 15 mm) for the turbulent condition. The data is constrained to the range of x = 162-198 mm to disregard non-physical rises at the intersection between the injector and the cover plate.

C. Correlation

For system design purposes, it is useful to define the cooling requirements necessary to reduce the peak heat transfer downstream of the shock interaction region to acceptable levels. Whilst, a full range of blowing ratios that reduce the wall heat transfer to or below the upstream turbulent/laminar levels have not been tested in this experimental campaign,

it is possible to correlate the experimental data concisely using a blowing parameter defined by the local inviscid conditions downstream of the re-compression shock (henceforth defined as the blowing parameter, $B_{h,s}$). This parameter has also been used by Holden and Sweet to correlate similar experimental data [7]. The blowing parameter is defined as

$$B_{h,s} = \frac{F_3}{St_3} = \frac{\dot{m}_f}{\rho_3 u_3} \cdot \frac{\rho_3 u_3 c_p (T_0 - T_w)}{\dot{q}_w} = \frac{\dot{m}_f c_p (T_0 - T_w)}{\dot{q}_w} \tag{7}$$

where St_3 is the Stanton number based on the boundary layer edge parameters downstream of the re-compression shock. These are defined by the subscript '3' from Fig 1. Based on this, Holden and Sweet correlated the heat transfer reduction downstream of the shock interaction region in turbulent flows [7] with the following expression

$$\frac{St}{St_{0,s}} = 1 - 0.92 \cdot \left[1 - \exp\left(- \frac{\left(\frac{\mathrm{M}_\infty}{\mathrm{M}_\mathrm{f}}\right) \cdot B_{h,s}}{4} \right) \right] \tag{8}$$

where $(\frac{\mathrm{M}_\infty}{\mathrm{M}_\mathrm{f}})$ is a molecular weight correction to account for the differing molecular weights of helium and nitrogen. This correlation was based on fitting a large number of test points with 5°, 7.5° and 10° shock generator angles at Mach 6 and 8 in which transpiration cooling was introduced with both nitrogen and helium gases. The molecular weight correction may be understood physically as akin to accounting for the differences in the volume of gas that is introduced. If it is assumed that on the porous injector, there is at least some coverage of coolant at all locations which are likely to be at the same temperature as the wall, then the major difference between injecting a heavier and lighter gas is the effect on the oncoming boundary layer. If the gas is lighter, it will take up more volume for a given mass flow rate and thus displace the boundary layer by a greater factor.

To correlate the experimental data, Fig 7 shows span-wise and stream-wise averaged (between y = -15 to 15 mm and x = 185-195 mm) Stanton number ratio ($St/St_{0,s}$) against the blowing parameter. From Fig 8a, there is a clear trend of increased cooling with higher blowing parameter with helium performing, as noted above, significantly better than nitrogen. A blowing parameter of approximately 0.4 leads to a heat reduction of 0.45 for helium as opposed to 0.85 for nitrogen. Both the transitional and turbulent cases show similar levels suggesting that as the shock interacts with the laminar boundary, there is a very rapid transition of the boundary layer to turbulence and therefore the region downstream of the shock impingement is fully turbulent. First of all, the experimental data from these tests may be compared directly to Holden's correlation, Eq. (8), as displayed in Fig 8b. There is reasonable agreement with the experimental measurements with the turbulent cases consistently under-predicting the level whilst transitional displays the opposite. The scatter in the points may be attributed either to the chosen molecular weight correction or the decision to compare both the transitional and turbulent cases against the same curve.

If the molecular weight correction is modified to include an exponent of 1.25, correlations with a better fit to the experimental data may be developed. Treating the transitional and turbulent cases separately, adjusted forms of Eq. (8)

may be fitted against the experimental results (Fig. 8c)

$$\frac{St}{St_{0,s}} = 1 - 0.92 \cdot \left[1 - \exp\left(-\frac{\left(\frac{\mathrm{M}_\infty}{\mathrm{M}_\mathrm{f}}\right)^{1.25} \cdot B_{h,s}}{4.75}\right)\right] \qquad \text{transitional} \tag{9}$$

$$\frac{St}{St_{0,s}} = 1 - 0.92 \cdot \left[1 - \exp\left(-\frac{\left(\frac{\mathrm{M}_\infty}{\mathrm{M}_\mathrm{f}}\right)^{1.25} \cdot B_{h,s}}{6.75}\right)\right] \qquad \text{turbulent} \tag{10}$$

where the factor 4 in the denominator of the exponential has been changed to 4.75 and 6.75 respectively for the transitional and turbulent cases. It is difficult to isolate the exact reason for the differences between the Holden and Sweet correlation and the two conditions tested in this study. It was noted by Holden that the experimental points for strong shock impingement with a 10° shock generator did not correlate as well as for lower shock strengths; the current experiment exclusively uses a 10° shock generator. From Fig. 5b, it appears that for the nitrogen cases in particular, the downstream heat transfer reduction continues to rise slightly from 185-200 mm. It is possible that in the 30 mm of length between the shock impingement location and the end of the injector, the flow field has not reached a fully turbulent condition. In addition, the differences in injector geometry and flow conditions may all have an impact on the cooling efficiency which would need to be explored either numerically or with a more detailed experimental parameter study. The choice of molecular weight correction, $(\frac{\mathrm{M}_\infty}{\mathrm{M}_\mathrm{f}})^{1.25}$, lies in between the correction factors for laminar, $(\frac{\mathrm{M}_\infty}{\mathrm{M}_\mathrm{f}})^{0.4}$, and turbulent, $(\frac{\mathrm{M}_\infty}{\mathrm{M}_\mathrm{f}})^{1.4}$, flows from prior experiments with the same porous injector and geometry without shock impingement [10]. Clearly, the thermal efficiency with dissimilar gas injection is tightly coupled to the nature of the external flow field. For example, whether it's laminar, turbulent, shock disturbed, etc. all require a different molecular weight correction. A complex, physics-based model is likely required to universally account for dissimilar gas injection for a broader range of external flow fields and injected gases.

Overall, it is encouraging that for both the fully turbulent and transitional cases, the peak heat fluxes can be reduced significantly with relatively small injection mass fluxes of nitrogen or helium. helium in particular proves to be more effective than previously suggested by Holden and Sweet. The empirical fits in Eqs. (9) and (10) may be used as a basis for simplified correlations to predict the peak heating for a given blowing rate for initial systems design.

Whilst these experiments have shown the potential benefits of applying transpiration cooling to cool regions of SWBLI, in a flight scenario instead of the heat flux reaching a peak with a cold wall, the wall temperature will rise to a steady level. At high temperatures, a further challenge in cooling these regions is viscosity-driven blockage where due to the higher viscosity at high temperatures, high plenum pressures are required to deliver a given mass flux compared to for a cold wall [25]. In fact, if the surface temperature is in the order of 2300 K, the viscosity increases by approximately four times for nitrogen injection, and therefore the injected mass flux reduces by the same factor assuming the external pressure is the same. This issue coupled with the high surface pressures at the shock-interaction region adds to the

overall challenge of transpiration cooling SWBLI regions.

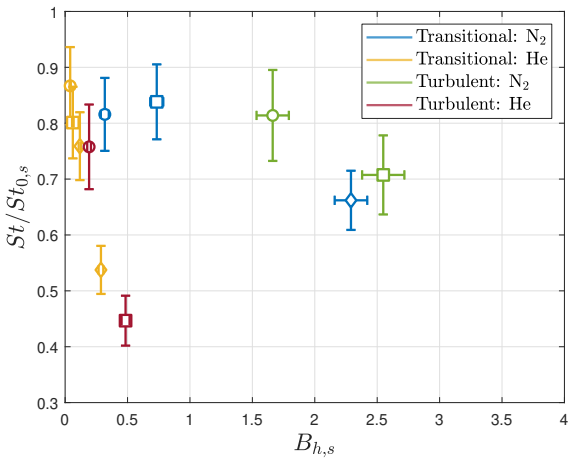

(a) No correction

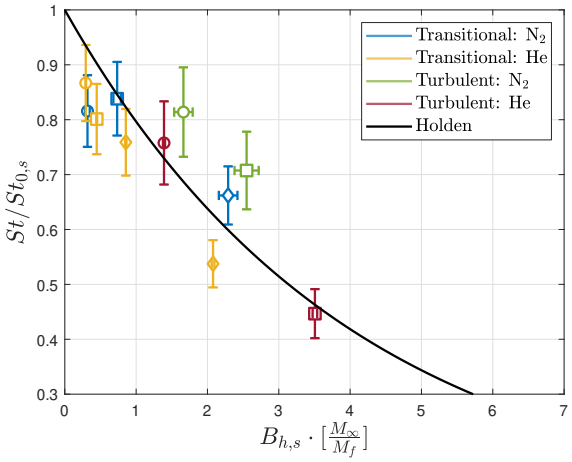

(b) With (M_∞/M_f) correction

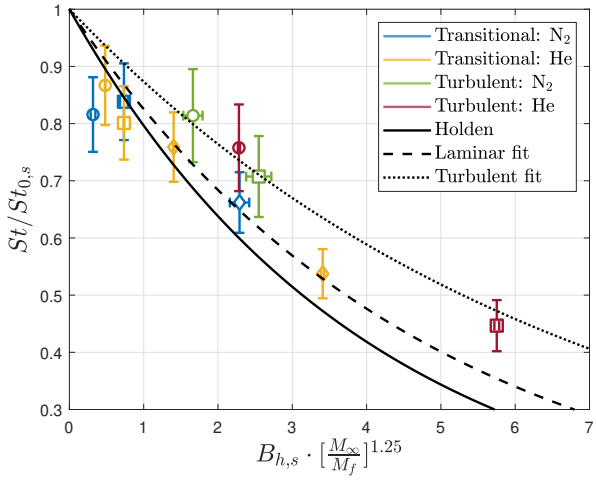

(c) With $(M_\infty/M_f)^{1.25}$ correction. The laminar-transional and turbulent fits refer to Eqs (9) and (10).

Fig. 8 Span-wise and stream-wise averaged (between y = -15 to 15 mm and x = 185-195 mm) Stanton number ratio ($St/St_{0,s}$) for transitional and turbulent case. The symbols correspond to different blowing rates from Fig 5 and 7 and the error bars to the uncertainty values presented in the Appendix.

IV. Conclusions

Cooling regions of peak heating caused by SWBLIs remain a topic of active research to this day. However, there is a lack of experimental data in the open literature exploring the effectiveness of transpiration cooling in mitigating heat transfer in regions of SWBLI, especially in the case of a transitional SWBLI which often produces the highest heat fluxes. In this paper, transpiration-cooling experiments have been conducted in the Oxford High Density Tunnel (HDT) to measure the surface heat transfer of a transpiration-cooled porous injector subjected to a strong oblique shock from a 10° shock generator.

For the laminar freestream condition, due to the strength of the incident shock, a transitional SWBLI region was formed with peak heating over 50 times greater than the nominal laminar level. The introduction of coolant injection led to a reduction in surface heat transfer for all cases. Relatively low blowing rates were sufficient to greatly reduce the heat transfer downstream of shock interaction with a blowing rate of 1.711% of nitrogen and 0.214% sufficient to reduce levels to 55-60% of the maximum in the transitional case. helium was significantly more effective than nitrogen with only 12.5% of the injected mass flux of helium sufficient to achieve a comparable heat flux reduction to nitrogen. The experimental data are correlated and both the transitional and turbulent cases display a similar trend. Two empirical fits have been proposed for the presented experimental data which can be valuable for aiding initial systems-level design for a transpiration-cooled system. In addition, the presented high-resolution, 2D heat transfer data can be useful validation tools to compare against high-fidelity CFD simulations in the future.

V. Acknowledgements

This research is funded by the EPSRC grant "Transpiration Cooling Systems for Jet Engine Turbines and Hypersonic Flight" (reference: EP/P000878/1). The authors would also like to thank the Reaction Engines and Engineering and Physical Sciences Research Council Collaborative Awards in Science and Engineering reward for supporting the studentship of Imran Naved. Gratitude is extended to Luke Doherty and Maïlys Buquet for running the experimental facilities, Chiara Falsetti for use of the infrared camera, and Hassan Saad Ifti for his efforts in designing the experimental model. Furthermore, the authors would like to thank the entire hypersonics group and the laboratory technical staff for their support and assistance over the course of this project. Lastly, the authors would like to extend their gratitude toward the reviewers who improved the quality of this paper.

References

[1] Babinsky, H., and Harvey, J. K., *Shock wave-boundary-layer interactions*, Cambridge University Press, 2011. doi:10.1017/CBO9780511842757.

[2] Knight, D., and Mortazavi, M., "Hypersonic shock wave transitional boundary layer interactions - A review," *Acta Astronautica*, Vol. 151, 2018, pp. 296–317. doi:10.1016/J.ACTAASTRO.2018.06.019.

[3] Currao, G. M. D., Choudhury, R., Gai, S. L., Neely, A. J., and Buttsworth, D. R., "Hypersonic Transitional Shock-Wave–Boundary-Layer Interaction on a Flat Plate," *AIAA Journal*, Vol. 58, No. 2, 2020, pp. 814–829. doi:10.2514/1.J058718.

[4] Hung, F., and Barnett, D., "Shockwave-boundary layer interference heating analysis," *AIAA 11th Aerospace Sciences Meeting*, American Institute of Aeronautics and Astronautics (AIAA), 1973. doi:10.2514/6.1973-237.

[5] Lunte, J., and Schülein, E., "Heat transfer amplification in transitional shock-wave/boundary-layer interactions," *AIAA Aviation 2019 Forum*, 2019, pp. 1–20. doi:10.2514/6.2019-3440, URL https://arc.aiaa.org/doi/10.2514/6.2019-3440.

[6] Sandham, N. D., Schülein, E., Wagner, A., Willems, S., and Steelant, J., "Transitional shock-wave/boundary-layer interactions in hypersonic flow," *Journal of Fluid Mechanics*, Vol. 752, 2014, pp. 349–382. doi:10.1017/JFM.2014.333.

[7] Holden, M. S., and Sweet, S. J., "Studies of transpiration cooling with shock interaction in hypersonic flow," *AIAA 25th Plasmadynamics and Lasers Conference, 1994*, American Institute of Aeronautics and Astronautics Inc, AIAA, 1994. doi:10.2514/6.1994-2475.

[8] Strauss, F., Witte, J., Weißwange, M., Manfletti, C., and Schlechtriem, S., "Experiments on shock-boundary layer interaction and cooling efficiency in a transpiration cooled model scramjet," *53rd AIAA/SAE/ASEE Joint Propulsion Conference, 2017*, 2017. doi:10.2514/6.2017-4833.

[9] Naved, I., Hermann, T., McGilvray, M., Ewenz Rocher, M., Hambidge, C., Doherty, L., Le Page, L., Grossmann, M., and Vandeperre, L., "Heat Transfer Measurements of a Transpiration Cooled Stagnation Point in Transient Hypersonic Flow," *Journal of Thermophysics and Heat Transfer*, 2022.

[10] Naved, I., Hermann, T., Hambidge, C., Falsetti, C., Saad Ifti, H., McGilvray, M., Elizarova, L., and Vandeperre, L., "Transpiration Cooling Heat Transfer Experiments in Laminar and Turbulent Hypersonic Flow," *Journal of Thermophysics and Heat Transfer*, 2022.

[11] Ifti, H. S., Hermann, T., McGilvray, M., Larrimbe, L., Hedgecock, R., and Vandeperre, L., "Flow Characterisation of Porous Ultra-High-Temperature Ceramics for Transpiration Cooling," *AIAA Journal*, 2022. doi:https://doi.org/10.2514/1.J061009.

[12] Oldfield, M. L., "Impulse response processing of transient heat transfer gauge signals," *Proceedings of the ASME Turbo Expo*, Vol. 3 PART A, American Society of Mechanical Engineers Digital Collection, 2006, pp. 739–750. doi:10.1115/GT2006-90949.

[13] Hermann, T., McGilvray, M., Ifti, H. S., Hufgard, F., and Löhle, S., "Thermal impulse response in porous media for transpiration-cooling systems," *Journal of Thermophysics and Heat Transfer*, Vol. 34, No. 2, 2020, pp. 447–456. doi:10.2514/1.T5841.

[14] McGilvray, M., Doherty, L. J., Neely, A. J., Pearce, R., and Ireland, P., "The Oxford High Density Tunnel," *20th AIAA International Space Planes and Hypersonic Systems and Technologies Conference, 2015*, AIAA American Institute of Aeronautics and Astronautics, 2015.

[15] Wylie, S., Doherty, L., and McGilvray, M., "Commissioning of the oxford high density tunnel (HDT) for boundary layer stability measurements at mach 7," *2018 Fluid Dynamics Conference*, 2018. doi:10.2514/6.2018-3074.

[16] Keyes, F. G., "The Heat Conductivity, Viscosity, Specific Heat and Prandtl Numbers for Thirteen Gases." Tech. rep., 1952.

[17] Eckert, E. R. G., "Survey of Boundary Layer Heat Transfer at High Velocities and High Temperatures," *Wright Air Development Center*, 1960.

[18] Schülein, E., "Skin Friction and Heat Flux Measurements in Shock/Boundary Layer Interaction Flows," *AIAA Journal*, Vol. 44, No. 8, 2006, pp. 1732–1741. doi:10.2514/1.15110.

[19] Heffner, K. S., Chpoun, A., and Lengrand, J. C., "Experimental study of transitional axisymmetric shock-boundary layer interactions at Mach 5," *AIAA 23rd Fluid Dynamics, Plasmadynamics, and Lasers Conference, 1993*, 1993. doi:10.2514/6.1993-3131.

[20] Ren, J., and Fu, S., "Secondary instabilities of Görtler vortices in high-speed boundary layer flows," *Journal of Fluid Mechanics*, Vol. 781, 2015, pp. 388–421. doi:10.1017/JFM.2015.490.

[21] Ifti, H. S., Hermann, T., McGilvray, M., and Merrifield, J., "Numerical Simulation of Transpiration Cooling in a Laminar Hypersonic Boundary-Layer," *Journal of Spacecraft and Rockets*, Vol. 59, No. 5, 2022, pp. 1726–1735.

[22] Keller, M. A., and Kloker, M. J., "Direct Numerical Simulation of Foreign-Gas Film Cooling in Supersonic Boundary-Layer Flow," *AIAA Journal*, Vol. 55, No. 1, 2016, pp. 99–111. doi:10.2514/1.j055115.

[23] Hombsch, M., and Olivier, H., "Film cooling in laminar and turbulent supersonic flows," *Journal of Spacecraft and Rockets*, Vol. 50, No. 4, 2013, pp. 742–753. doi:10.2514/1.A32346/ASSET/IMAGES/LARGE/FIGURE27.JPEG.

[24] Arnal, D., and Délery, J., "Laminar-Turbulent Transition and Shock Wave/Boundary Layer Interaction," *RTO-EN-AVT-116 — Critical Technologies for Hypersonic Vehicle Development*, 2004, pp. 1–46.

[25] Langener, T., Wolfersdorf, J. V., and Steelant, J., "Experimental Investigations on Transpiration Cooling for Scramjet Applications Using Different Coolants," *AIAA Journal*, Vol. 49, No. 7, 2011, pp. 1409–1419. doi:10.2514/1.j050698.

[26] Coleman, H. W., and Steele, W. G., *Experimentation, Validation, and Uncertainty Analysis for Engineers: Third Edition*, John Wiley and Sons, Hoboken, NJ, USA, 2009. doi:10.1002/9780470485682.

[27] Astarita, T., and Carlomagno, G. M., *Infrared Thermography for Thermo-Fluid-Dynamics*, Springer Berlin Heidelberg, 2013. doi:10.1007/978-3-642-29508-9.

VI. Uncertainty Analysis

The main independent quantities reported in this paper are the Stanton number, the blowing ratio, the blowing parameter and the unit Reynolds number. To find the total uncertainty, the Taylor Series Method by Coleman and Steele [26] was employed where, for a function $r = r(X_1, X_2, ...X_n)$, the uncertainties in the individual measurements are assumed to be uncorrelated. Thereafter, gradients $\frac{\partial r}{\partial X_i}$ are calculated numerically by perturbing the variables X_i in the data reduction processing steps. First of all, the unit Reynolds number is calculated according to the following equation

$$Re_u = \frac{\rho_e u_e}{\mu_e} \tag{11}$$

where u_e and ρ_e are a function of the Mach number, M, total pressure, P_0, and total temperature, T_0. The Stanton number is calculated according to Eq X where the heat flux at the wall, $\dot{q}_w$, is a function of the material thermal

effusivity, $\sqrt{\rho c_p k}$, and the temperature, T_w, obtained through infrared camera measurements. The blowing ratio is calculated using Eq. (3), which depends on T_e and ρ_e as well as the injected mass flux, $\rho_f u_f$. This is calculated assuming a linear pressure gradient through the porous injector and a constant solid temperature by employing Eq. (2). The uncertainties in the Darcy and Forchheimer coefficients were determined using the same monte carlo simulation procedure detailed in Ref [11].

The wall temperature, T_w is determined via infrared thermography and a key figure of merit used to qualify the temperature output of infrared cameras is the noise equivalent differential temperature (NETD) [27]. In this work, a factory calibration determined that the NETD was below 40 mK over the observed range of temperatures. This is significantly smaller than the expected temperature rise of the injector of 0.5-10 K. In addition to the NETD, there are additional sources of error from the infrared calibration system. This includes the uncertainties in the measurement of the reflected temperature when conducting the multipoint calibration, T_{ref}, the error in the temperature measurement of the CI-Systems black body calibrator, $T_{\text{calibrator}}$, and the emissivity of the material, ε.

Table 4 details the different uncertainty contributions to the overall uncertainty in the measurement of Reynolds number, Stanton number, blowing ratio, and blowing parameter for the case of an injected mass flux of 0.81 $\text{kg s}^{-1}\,\text{m}^{-2}$. The main drivers of uncertainty, especially for the Stanton number and blowing parameter are the total temperature, T_0, and the material thermal effusivity. The uncertainty in the blowing parameter is 11.4% where the main source of uncertainty is the total temperature (60%). In future experiments, the uncertainty may be reduced with a tighter measurement of total temperature and higher accuracy measurements of material thermophysical properties.

Table 4 Uncertainty contributions and overall uncertainties in unit Reynolds number, uncooled Stanton number, blowing ratio and blowing parameter for the laminar freestream condition with nitrogen injection at $0.81\,\mathrm{kg\,s^{-1}\,m^{-2}}$ and a METAPOR CE170 injector.

Parameter	Baseline value	Absolute uncertainty	Relative uncertainty
NETD / K	0.04	±0.02	50%
T_{ref} / K	296	±2	<1%
$T_{\mathrm{calibrator}}$ / K	296	±0.1	<1%
ε	0.95	±0.04	4.2%
$(\sqrt{\rho c_p k})$ / $\mathrm{Jm^{-2}K^{-1}s^{-0.5}}$	1565	±78.25	5%
P_0 / kPa	1204	±24.08	2%
T_0 / K	420	±10	2.4%
M	6.1	±0.1	1.6%
T_{pl} / K	293	±2	<1%
p_{pl} / K	$3.89 \cdot 10^5$	$\pm 1 \cdot 10^4$	2.5%
K_D / $\mathrm{m^2}$	$2.52\,/\,\mathrm{m} \cdot 10^{-13}$	$\pm 1.74 \cdot 10^{-14}$	6.9%
K_F / m	$1.03\,/\,\mathrm{m^2} \cdot 10^{-8}$	$\pm 1.06 \cdot 10^{-9}$	10.3%
Re_u / m^{-1}	$13.3 \cdot 10^6$	$6.26 \cdot 10^5$	4.7%
St_0	$5 \cdot 10^{-3}$	$6.62 \cdot 10^{-4}$	13.2%
F	$1.72 \cdot 10^{-2}$	$1.24 \cdot 10^{-3}$	7.2%
$B_{h,s}$	2.3	0.27	11.4%